Bilayer h-BN barriers for tunneling contacts in fully-encapsulated monolayer MoSe2 field-effect transistors

Ghiasi, Talieh S.; Quereda , Jorge; van Wees, Bart J.

Published in:
2D Materials

DOI:
10.1088/2053-1583/aadf47

PAPER • **OPEN ACCESS**

Bilayer h-BN barriers for tunneling contacts in fully-encapsulated monolayer $MoSe_2$ field-effect transistors

To cite this article: Talieh S Ghiasi *et al* 2019 *2D Mater.* **6** 015002

2D Materials

OPEN ACCESS

RECEIVED
4 June 2018

REVISED
12 August 2018

ACCEPTED FOR PUBLICATION
6 September 2018

PUBLISHED
5 October 2018

PAPER

Bilayer h-BN barriers for tunneling contacts in fully-encapsulated monolayer $MoSe_2$ field-effect transistors

Talieh S Ghiasi, Jorge Quereda and Bart J van Wees

Zernike Institute for Advanced Materials, University of Groningen, Groningen, 9747 AG, Netherlands

E-mail: t.s.ghiasi@rug.nl

Keywords: monolayer molybdenum diselenide ($MoSe_2$), tunneling contact, bilayer hexagonal boron nitride (h-BN), BN-encapsulation, field-effect mobility

Supplementary material for this article is available online

Abstract

The performance of electronic and spintronic devices based on two-dimensional semiconductors (2D SC) is largely dependent on the quality and resistance of the metal/SC electrical contacts, as well as preservation of the intrinsic properties of the SC channel. Direct metal/SC interaction results in highly resistive contacts due to formation of large Schottky barriers and considerably affects the properties of the 2D SC. In this work, we address these two important issues in monolayer $MoSe_2$ field-effect transistors (FETs). We encapsulate the $MoSe_2$ channel with hexagonal boron nitride (h-BN), using bilayer h-BN at the metal/SC interface. The bilayer h-BN eliminates the metal/$MoSe_2$ chemical interactions, preserves the electrical properties of $MoSe_2$ and reduces the contact resistances by prevention of Fermi-level pinning. We investigate electrical transport in the monolayer $MoSe_2$ FETs that yields close to intrinsic electron mobilities ($\approx 26\,cm^2\,V^{-1}\,s^{-1}$) even at room temperature. Moreover, we experimentally study the charge transport through metal/h-BN/$MoSe_2$ tunnel contacts and we explicitly show that the dielectric bilayer of h-BN provides highly efficient gating (tuning the Fermi energy) of the $MoSe_2$ channel at the contact regions even with small biases. Also we provide a theoretical model that allows to understand and reproduce the experimental I–V characteristics of the contacts. These observations give an insight into the electrical behavior of the metal/h-BN/2D SC heterostructure and introduce bilayer h-BN as a suitable choice for high quality tunneling contacts that allows for low energy charge and spin transport.

1. Introduction

Atomically thin transition metal dichalcogenides (TMDs) are among the most promising materials for nano-electronics. In particular, single-layer TMDs can be used as a high-mobility semiconductor channel in field effect transistors (FETs), yielding significant on/off current ratios ($I_{on}/I_{off} > 10^8$) [1] and reduced power dissipation [2]. In recent years, the coupled spin-valley physics in TMDs [3] has also attracted broad attention, since it provides a new opportunity for (opto-) spin-valleytronic applications [4, 5].

A major challenge for efficient charge and spin transport in TMD-based FETs is to achieve high quality, low resistive electrical contacts at the source and drain electrodes [6–14]. Direct metal/TMD interaction causes Fermi-level pinning and formation of large Schottky barriers and affects the electrical properties of the 2D TMD layer [15, 16]. Also, the atomic thickness of the 2D channel falls below the width of the charge depletion region at the metal/TMD contact. These facts lead to highly resistive electrical contacts that significantly limits the charge injection/detection efficiency in these FETs.

An effective strategy to address these issues is to use an insertion layer in between the TMD and metal, such as MgO, TiO_2, Ta_2O_5 and h-BN [7, 9, 10, 11–14]. Among them, h-BN is more promising for 2D contacts with TMDs since deposition of other mentioned materials on the dangling bond-free surface of TMD can lead to formation of isolated atomic islands and therefore poor quality of the contacts.

Further, it was shown that bilayer h-BN tunnel barriers are highly efficient for spin injection [17]. This is not the case for monolayer h-BN, since it provides the SC channel with ohmic contacts [9] due to chemisorption of the h-BN to the metal (e.g. Ti and Co) [18] which might cause conductivity mismatch

problem that considerably restrains the spin injection efficiency [19].

To our knowledge, a detailed description of the electrical behavior of metal/bilayer h-BN contacts for monolayer $MoSe_2$ FETs is yet to be provided. In this work, we use an exfoliated bilayer h-BN as a tunnel barrier between the $MoSe_2$ channel and the Ti electrodes that disrupts the metal/TMD chemical interactions [20, 21]. Also, as recently reported [18], the chemisorption of h-BN to Ti, lowers the Ti workfunction by 0.78 eV, improving its band alignment with the $MoSe_2$ conduction band.

Using a theoretical model for the electrical behavior of the metal/h-BN/TMD contacts, we are able to describe and reproduce the experimental observations in the three-terminal *I–V* characteristics. In particular, we show that the strong out-of-plane electric fields formed at the contact interface can considerably modulate the doping of the underlying channel.

We also evaluate the electrical performance of the monolayer $MoSe_2$. The charge transport studies to date on monolayer $MoSe_2$ FETs are limited to two-terminal measurements on non-encapsulated channels [22, 23]. However, in this work, the use of metal/h-BN electrodes, instead of direct metal/TMD contacts, allows for full h-BN encapsulation of the $MoSe_2$ channel that reduces the effect of (impurity dependent) Coulomb and roughness scatterings [24, 25] and prevents degradation of the $MoSe_2$ crystal [26]. As further discussed below, the FETs are fabricated using a contact geometry that reduces the interaction between the electrodes and the channel. Thus, we can expect our four-terminal measurements to reflect the intrinsic behavior of the monolayer $MoSe_2$ at room temperature.

Figure 1 shows a sketch and an optical microscope image of the studied FETs. In these devices the monolayer $MoSe_2$ channel is encapsulated between bilayer and bulk h-BN as the top and bottom flakes, respectively. The h-BN/$MoSe_2$/h-BN heterostructure is stacked on a SiO_2(300 nm)/doped Si substrate, using a dry pick up technique [27] which provides polymer-free interfaces. The Ti (5 nm)/Au (75 nm) electrodes are fabricated by e-beam lithography (EBL), followed by e-beam evaporation of the metals at UHV (see methods for details). The choice of Ti for the electrodes in these devices is due to its low work-function (4.33 eV) which closely matches the electron affinity of a monolayer $MoSe_2$ ($E_C = 3.99$ eV) [28].

Our sample contains two devices that are numbered in the optical image of figure 1(b). Device 1 and 2 address the separate 1L-$MoSe_2$ flakes which are covered with 2- and 5-layer h-BN, respectively. A homogeneous bulk h-BN flake is used as bottom layer in both devices and the doped Si layer is used as a back-gate electrode.

2. Two-terminal measurements

We start with evaluation of the FET performance by two-terminal (2T) measurements. All the measurements are done at room temperature and in vacuum ($<10^{-4}$ mbar). As shown in the device sketches of figure 2, the SC channel is connected to the source and drain electrodes through the top h-BN layers and is separated from the gate electrode by the bulk h-BN and SiO_2. The source electrode is grounded and a voltage (V_{sd}) is applied on the drain electrode, while measuring the source-drain current (I_{sd}). We measure I_{sd} as a function of gate voltage (V_g) (transfer curve) at different V_{sd} for the both devices of 1 and 2 (figures 2(a) and (b)) that shows gate-modulation of channel conductivity by tuning the density of charge carriers in the $MoSe_2$ channel.

The transfer curves show an almost hysteresis-free charge transport. The I_{sd} increases for V_g larger than the threshold voltage (V_{th}), as the Fermi energy approaches the conduction band minimum (E_C). Comparison of the 2T measurements performed in device 1 and 2 shows that the 2T current injected through 2L h-BN is much larger than the current injected through 5L h-BN. From this 2T current ratio and square resistance of the channel (measured in four-terminal geometry, see next section), we estimate that the resistance of the contacts with 5L h-BN is 4 orders of magnitude larger than the ones with 2L h-BN. This observation is consistent with the fact that the increase in the number of h-BN layers reduces the charge tunneling efficiency into the channel [29] but does not show considerable improvement in lowering the Schottky barrier height [14].

The 2T source-drain *I–V* measurements (figures 2(c) and (d)), show the non-linear, almost symmetric behavior, indicating the dominance of the contacts in the 2T charge transport (otherwise we would expect linear *I–V* characteristics). In the SD *I–V* curves of device 2 (figure 2(d)), we observe that I_{sd} starts to saturate at large V_{sd}. This saturation can be attributed to the 'pinch-off' region in the SC channel, because the applied V_{sd} acts as a gate and can create a depletion region in the channel close to the drain contact [30]. The saturation of the current at such low SD biases shows that these contacts can considerably gate the channel. The V_{sd} at which the saturation of current happens, depends on the density of charge carriers in the channel. The higher V_g, induces a larger density of charge carriers and therefore charge depletion close to the contacts happens at larger V_{sd}.

Therefore, the electrical performance of a two-terminal TMD-based FET is highly dependent on the electrical response of the contacts. When the metal comes in vicinity of the n-type 2D SC, the SC gets charge-depleted [15]. In figure 2(e), we show the schematic drawings of the metal/h-BN/SC interface, where the black gradient illustrates the depleted region that is gradually disappearing in the lateral direction of the SC along the channel. The corresponding band diagram shows the only energy level available for the states in the 2D SC channel beneath the contact (region A) which reaches the less depleted region close to the

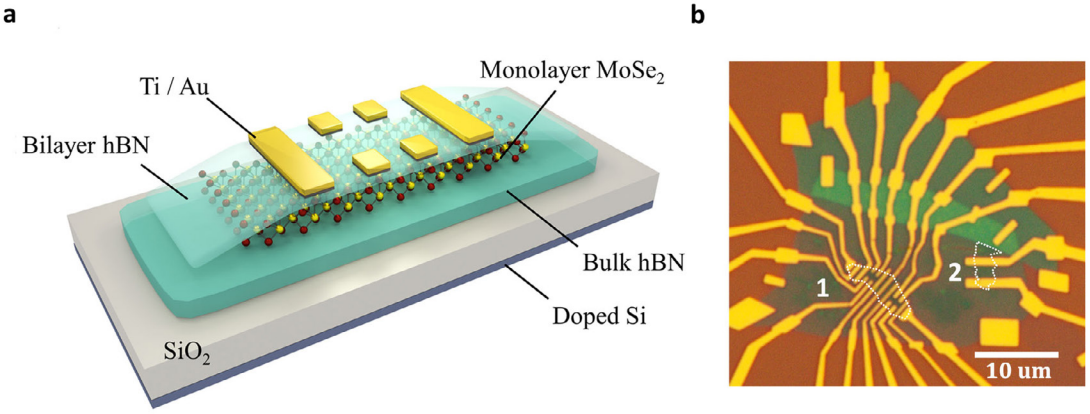

Figure 1. Device geometry. (a) Sketch of the BN-encapsulated 1L $MoSe_2$ FET with Ti/Au contacts. (b) Optical microscope image of the fabricated device. The edges of the separate $MoSe_2$ flakes are shown by the white dashed lines. In device 1 and 2, the $MoSe_2$ flakes are covered with 2-layer and 5-layer h-BN, respectively.

edge of the contact (region B) and laterally expands into the SC where there will be no charge depletion and the SC bands preserve their intrinsic energy levels (region C) [15]. In this situation the charge carriers that are injected far from the edge of the contact, firstly encounter region A before reaching region B. The low density of charge carriers at these depleted regions makes the contact areas highly resistive in comparison with the channel. Therefore, in the 2T measurements, modulation of the I_{sd} as a function of V_{sd} and V_g is considerably affected by the contact regions that have the main contribution in the voltage drop in the 2T circuit. In the band diagram of figure 2(e), we also show the tunnel barrier formed by the van der Waals (vdW) gap in addition to the h-BN layer. This gap might not be present in the direct metal/TMD interface, since the interaction can be accompanied with covalent bonding (strong hybridization) [31].

We also compare the performance of the 2T FETs, fabricated with encapsulated and non-encapsulated 1L-$MoSe_2$ channels (see supplementary information (SI) (stacks.iop.org/TDM/6/015002/mmedia), section 3). We observe that the BN-encapsulation of the channel considerably improves the 2T electrical transport in the 1L-$MoSe_2$. This is because TMDs are highly sensitive to environmental adsorbates or scattering centers [32]. This fact, in addition to the formation of large SB at the direct metal/TMD interface leads to one order of magnitude lower 2T conductivity and mobility in the non-encapsulated $MoSe_2$ channel. Also there is a large hysteresis in the electrical measurements on non-encapsulated $MoSe_2$ FET (about 29 V), while the BN-encapsulated sample shows almost no-hysteresis for the same gate bias sweeping rate.

3. Four-terminal measurements

In order to investigate the intrinsic electrical properties of the monolayer $MoSe_2$ channel, we perform four-terminal (4T) measurements. As shown in the device sketches of figure 3, we apply the V_{sd} to the outer electrodes and measure I_{sd}, while probing the voltage drop across the inner electrodes (V_{4T}). First, we perform these measurements with the electrodes that are crossing the full width of the channel (crossing electrodes). Figure 3(a) shows the dependence of channel conductivity ($\sigma = I_{sd}L_{ch}V_{4T}^{-1}W_{ch}^{-1}$) on V_g. This n-type behaviour indicates that the Fermi level of the SC is closer to its conduction band. Figure 3(c) shows the linear dependence of V_{4T} on I_{sd}. From the slope of the SD I–V curves, we extract the square resistance (R_{sq}) of the channel at different V_g ($R_{sq} = 0.5$ MΩ to 1.5 MΩ for the range of $V_g = 60$ V to 45 V).

However, the depleted regions of the contact areas (shown in figure 2(e)) can contribute to the 4T measurements, performed by using the crossing contacts. In order to avoid the effect of the depleted regions and address the intrinsic electrical behavior of the channel material, we perform the 4T measurements using side contacts (the electrodes that are partially covering the channel). The minimized overlap of the side contacts with the $MoSe_2$ flake diminishes screening of the gate-induced charges in the channel. Figure 3(b) shows the measurement geometry and gate dependency of the channel conductivity. The dependence of V_{4T} as a function of I_{sd} for different V_g is shown in figure 3(d). The considerable difference between the results of these two 4T measurement geometries (figures 3(a) and (b)) makes it clear that the role of the mentioned depleted regions underneath the contacts should not be overlooked. The conductivity of the channel, derived from the 4T measurements with the side contacts, clearly shows linear behavior for $V_g > V_{th} = 20$ V, while the conductivity measurements with the crossing contacts are behaving more similar to the 2T measurements (figure 2(a)) that show gradual increase versus V_g and hardly reaches the linear regime. By the linear fit to the conductivity curve for $V_g > V_{th}$ (in figure 3(b)), we extract the electron field-effect mobility of $\mu_{FE} \approx 26$ $cm^2\ V^{-1}\ s^{-1}$, considering the effective width of the channel since it is partially covered by the side contacts.

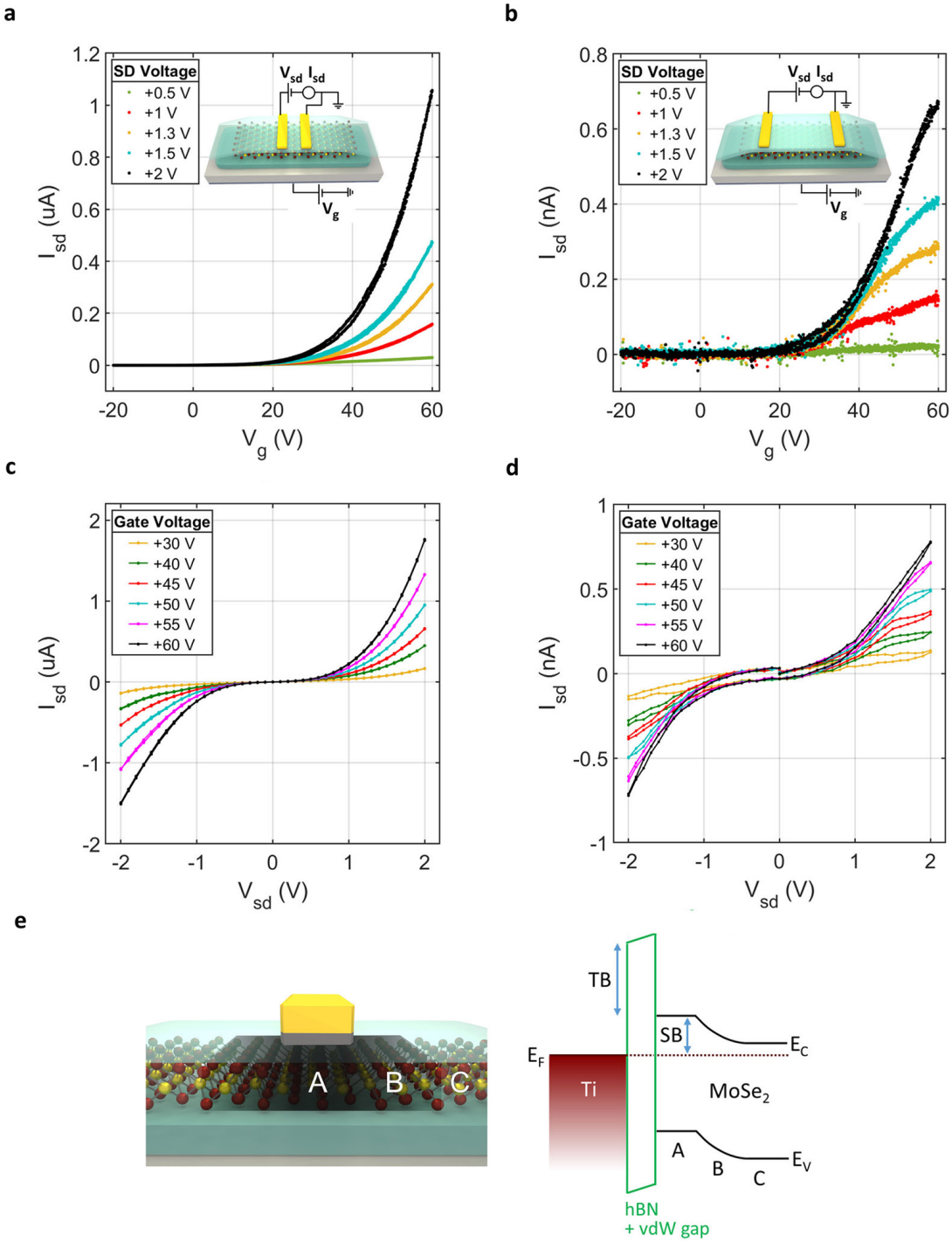

Figure 2. Two-terminal electrical measurements. (a) and (b) Source-drain (SD) current (I_{sd}) as a function of gate voltage (V_g) measured at different SD biases (V_{sd}) on (a) 1L-$MoSe_2$ (channel length of $L_{ch} = 0.93\,\mu$m and channel width of $W_{ch} = 2.8\,\mu$m), covered with 2 layers of h-BN and (b) 1L-$MoSe_2$ (with $L_{ch} = 2.54\,\mu$m and $W_{ch} = 1.6\,\mu$m), covered with 5 layers of h-BN. Sketches of the device and measurement geometry are shown in the insets. (c) and (d) SD I–V characteristics at different V_g for the FETs with 2L (c) and 5L (d) h-BN. (e) Schematic drawing and the corresponding band diagram of a Ti/h-BN/$MoSe_2$ heterostructure. The black gradient below the contact illustrates the highly depleted region (A) underneath the contact that extends laterally in the 2D SC through region (B) until it reaches the non-depleted region (C).

The extracted μ_{FE} in the 1L-$MoSe_2$ channel is close to the intrinsic value predicted by theoretical studies [33]. This indicates that the electrical properties of the channel are well preserved in our sample. The BN-encapsulation of the channel reduces the Coulomb scatterings caused by charged impurities at the interfaces or on the channel surface (e.g. fabrication residues) and also eliminates roughness scatterings originating from the Si substrate [34, 35] that could highly affect the charge carrier mobility [36, 37]. From the linear I–V curves measured with the side contacts, we extract the values of $R_{sq} = 130\,\text{k}\Omega$ to $190\,\text{k}\Omega$ for the range of $V_g = 60\,\text{V}$ to $45\,\text{V}$. The channel resistances is about 1 order of magnitude smaller than the ones measured with the crossing contacts. The derived R_{sq} and μ_{FE} are consistent with the results of the same measurements done

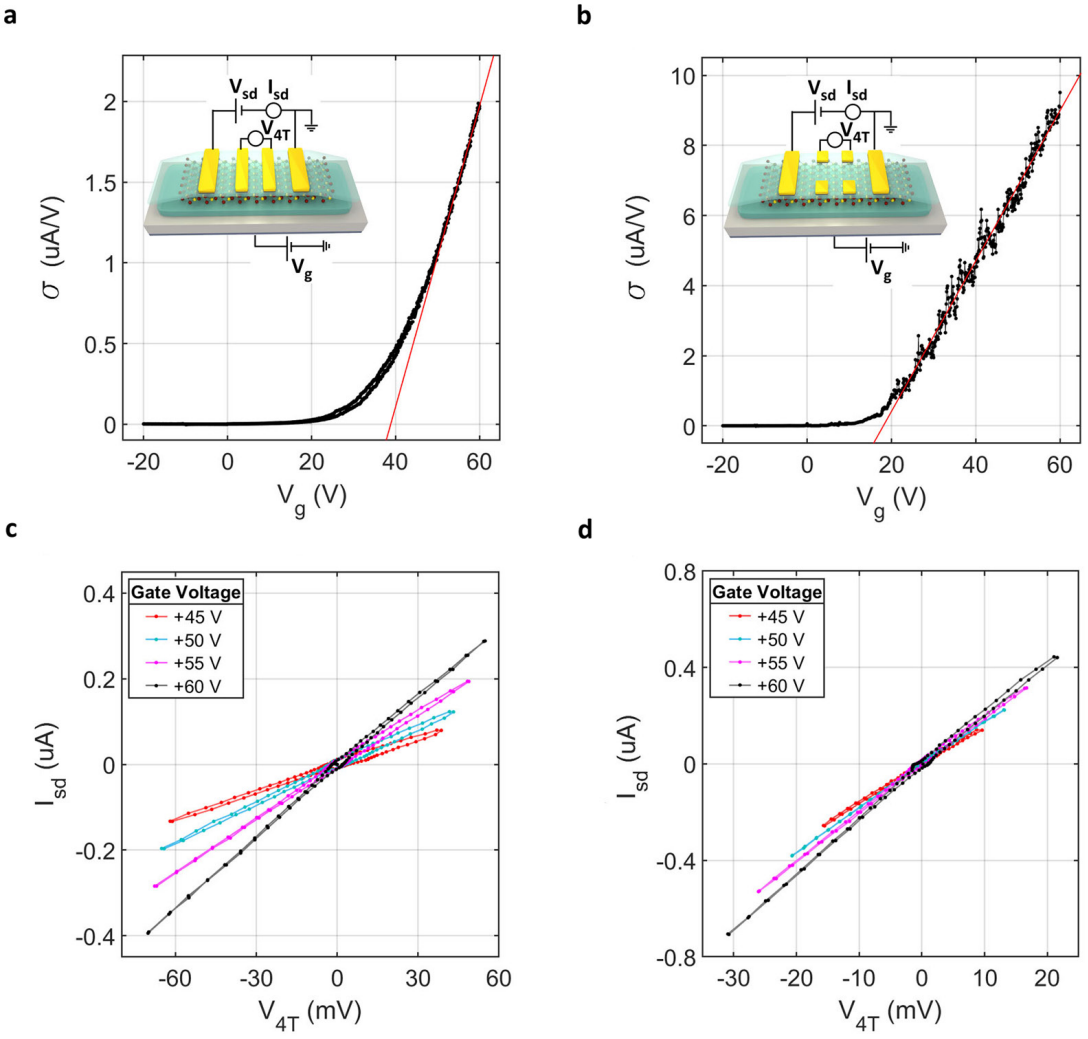

Figure 3. Four-terminal electrical characterization of the BN-encapsulated $MoSe_2$ channel. (a) and (b) Channel conductivity (σ) for the device with bilayer h-BN tunnel barrier as a function of V_g, where the four-terminal voltage (V_{4T}) was measured using (a) electrodes that fully cover the channel (crossing electrodes) and (b) using side electrodes. The insets are sketches of the device and measurement geometries. (c) and (d) Four-terminal I–V characteristics at different gate voltages (V_g) as measured with the crossing (c) and the side (d) electrodes.

with the other pairs of side contacts (see figure 1(b)). In contrast, the 4T measurements performed with the crossing electrodes vary for different contacts along the channel because of the inhomogeneity of the contact regions (can be due to the presence of bubbles at the 2D interfaces or variation of the contact area). This observation is another evidence for contribution of the depletion regions from the crossing contacts in the latter case.

4. Modeling of metal/h-BN/TMD tunnel contact and three-terminal measurements

As shown, the performance of the TMD-based FETs is largely affected by the contact regions. We model the electrical behavior of the contacts using the band diagram of the metal/h-BN/TMD heterostructure shown in figure 4. The system can be conceptually understood as a parallel-plate capacitor with a small leakage current (tunneling through the h-BN). When the applied voltage between the metal and $MoSe_2$ is zero (figure 4(a)), the Fermi levels at the metal and $MoSe_2$ are the same, $E_{F,M} = E_{F,S}$. The band alignment between h-BN and $MoSe_2$ will be determined by the difference between their electron affinities ($\chi_{MoSe_2} - \chi_{BN}$). At the metal side, the band alignment will be given by the difference between the electron affinity of h-BN and the work function of titanium ($\phi_M - \chi_{BN}$). We consider ϕ_M shifted by 0.78 eV due to the chemisorption of h-BN to Ti [18]. The position of $E_{F,S}$ with respect to E_C is controlled by the gate voltage. Importantly, the matching of the Fermi energies between Ti and $MoSe_2$ at equilibrium requires a misalignment of the vacuum levels at the two sides of the h-BN barrier. Thus, even at zero applied bias, a nonzero electrostatic voltage drop V_{BN} will appear at the h-BN layer.

V_{3T} is the voltage drop across the tunnel barrier which is the difference between the Fermi energies of the metal and semiconductor. When $V_{3T} \neq 0$ (see figures 4(b)–(d)), the Fermi energies at both sides become misaligned by $E_{F,M} - E_{F,S} = qV_{3T}$ where $-q$

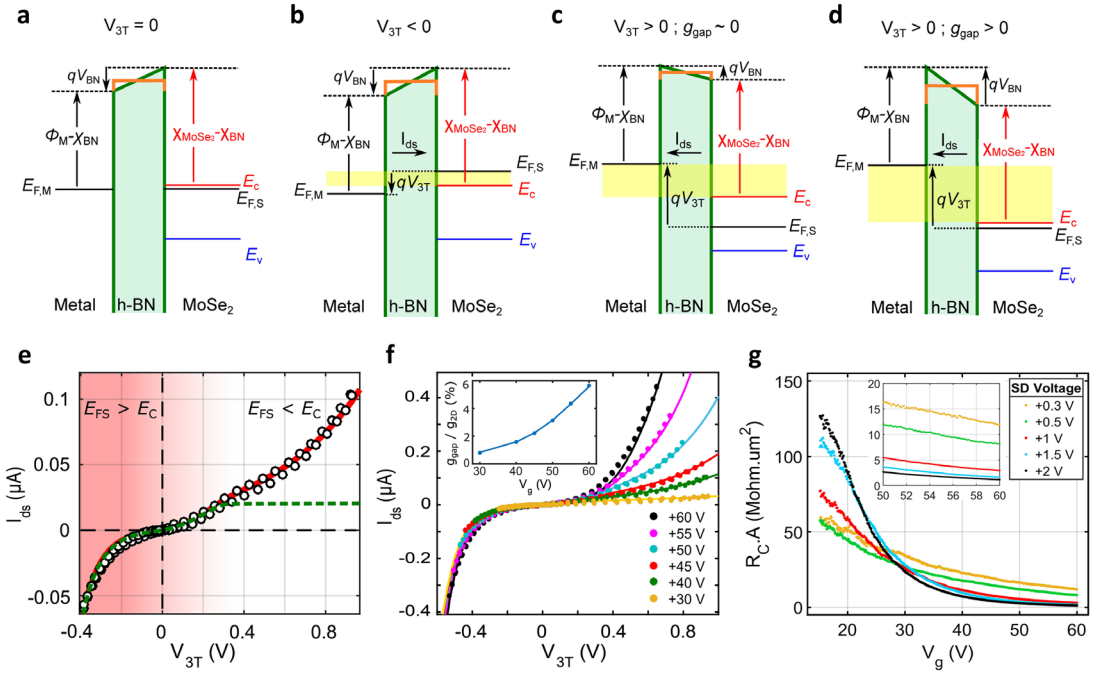

Figure 4. Model for the metal/h-BN/TMD tunnel contact. ((a)–(d)) Band diagrams of the tunnel contact for (a) $V_{3T} = 0$, (b) $V_{3T} < 0$, (c) $V_{3T} > 0$ and $g_{gap} \sim 0$ and (d) $V_{3T} > 0$ and $g_{gap} > 0$. (e) Experimental three-terminal I–V characteristic of the contact for $V_g = 40$ V and fit to the model (red solid line). The green dashed line shows the calculated tunneling I–V with $g_{gap} = 0$. (f) Fit (solid lines) to the experimental three-terminal I–V characteristics (circles) at different gate voltages. The A and B parameters (see equation (3)), as well as V_{th} are kept constant for the full set of I–V curves. V_g is matched with the experimental applied voltages and g_{gap} is used as the only fitting parameter. Inset: g_{gap}, extracted from the fittings as a function of the gate voltage. (g) Product of contact resistance and area ($R_C \cdot A$) as a function of V_g, measured at different SD biases. The inset shows modulation of $R_C \cdot A$ in the zoomed-in range of V_g.

is the electron charge. Then, owing to the capacitive coupling between metal and $MoSe_2$, the charge density of $MoSe_2$ changes. Due to the limited density of available states, this will cause a shift in the position of the edge of the conduction band with respect to $E_{F,S}$. From the band diagrams of figure 4, one gets the relation

$$qV_{BN} - qV_{3T} = \phi_M - \chi_{MoSe_2} + (E_{F,S} - E_C). \quad (1)$$

In order to clarify the meaning of equation (1), we now consider two situations. First, let us assume that the density of states at the $MoSe_2$ near $E_{F,S}$ is large (e.g. when the Fermi energy is well inside the conduction band of $MoSe_2$, figure 4(b)). Then, when the three-terminal voltage is increased by ΔV_{3T}, charge carriers can accumulate in the $MoSe_2$ layer by filling empty states without noticeably shifting $E_{F,S}$ with respect to E_C, $\Delta(E_{F,S} - E_C) \simeq 0$ and, from equation (1), $\Delta V_{BN} \simeq \Delta V_{3T}$. Thus, the shape of the h-BN tunnel barrier, as well as the energy window at which electrons can tunnel through the barrier (highlighted in yellow in figure 4(b)) are strongly dependent on V_{3T}. On the other hand, if the density of states at the $MoSe_2$ near the Fermi energy is very low (i.e. when $E_{F,S}$ is inside the bandgap, figure 4(c)), charge can only be accumulated (or removed) by largely shifting $E_{F,S}$ with respect to E_C. In this case, the shape of the h-BN barrier and the tunneling energy window are barely affected by changing V_{3T}. Thus, the tunneling current through the barrier becomes saturated (For extended discussion on the influence of the gap states see SI, section 6).

Next, we use the band diagrams discussed above to model the tunneling I–V characteristic of the h-BN barrier. The tunneling current density, J_{tunnel} is approximately given by [38]

$$J_{tunnel} = A \times \sum_{\text{all bands}} 2 \int g_{2D} \times P_{tunnel}(E) \times (f(E - E_F) - f(E - E_F - V_{3T}))\, dE \quad (2)$$

where we model the $MoSe_2$ density of states as that of a 2D electron gas, $g_{2D} = m_e^*/(\pi\hbar^2)$. P_{tunnel} is the transmission probability through the h-BN barrier, f is the Fermi–Dirac distribution function and the sum runs for all the spin–orbit split subbands. A is a contact-dependent fitting parameter to be empirically determined. The factor 2 before the integrals accounts for the valley degeneracy. For simplicity, we approximate the trapezoidal tunnel barrier (indicated in green in the band diagrams of figure 4) by a rectangular barrier with an effective barrier height equal to the average height along the h-BN (orange line in the diagrams). We further assume that P_{tunnel} is exponentially dependent on the energy of the tunneling electrons as

$$P_{tunnel}(E) = \exp\left(\frac{-B\sqrt{2m^*}}{\hbar} \times \sqrt{U_{barrier} - E}\right) \quad (3)$$

where $U_{barrier} = \chi_{MoSe_2} - \chi_{BN} + \frac{1}{2}qV_{BN}$ is the tunneling barrier height and E is the electron energy

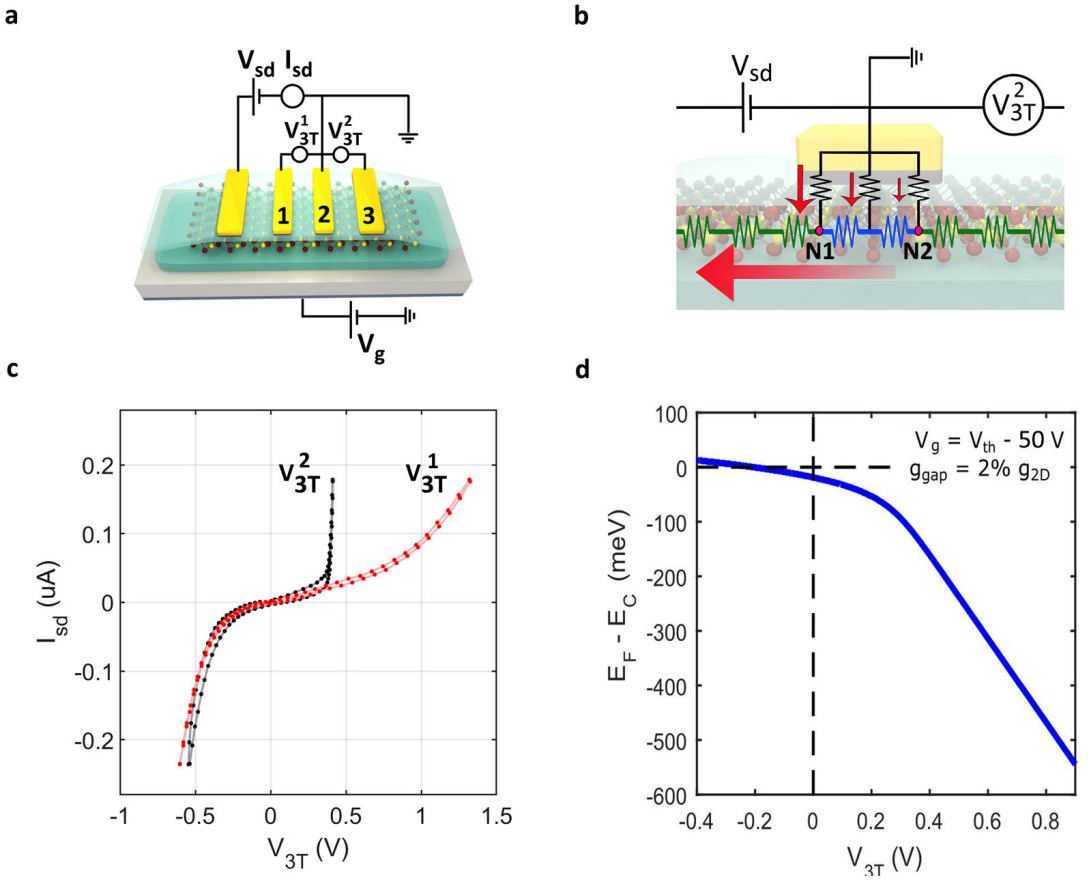

Figure 5. Effect of current crowding on three-terminal measurements. (a) Sketch of the device and 3T measurement geometries. (b) Resistor network at the metal/h-BN/TMD interface and the TMD channel. Red arrows depict the electron current and illustrate current crowding at the contact region. (c) Comparison of V_{3T}^1 and V_{3T}^2, measured as a function of I_{sd} at $V_g = +50$ V in the geometry shown in panel (a). (d) Modulation of Fermi energy of $MoSe_2$ as a function of the 3T voltage, assuming a nonzero density of gap states and a back gate voltage of $V_g = V_{th} - 50$ V in the model.

with respect to $E_C \cdot B$, similar to A in equation (2), is used as a contact-dependent fitting parameter. Note that, for the case of isotropic, parabolic bands one gets $B = 1$, while we get the best fit to our experimental data considering $B = 0.3$. Figure 4(e) shows the fit (red line) to an experimental three-terminal I–V (markers) with $V_{gate} = 40$ V. The I–V characteristic can be divided in two different regimes, depending on whether the $E_{F,S}$ is above (figures 4(a) and (b)) or below (figures 4(c) and (d)) E_C. For $E_{F,S} > E_C$, the density of states at the $MoSe_2$ is large. Thus, the barrier height $U_{barrier} \propto V_{BN}$ will change almost linearly with V_{3T}. For $E_{F,S} < E_C$, however, the density of states becomes much lower. Thus, $U_{barrier}$ changes more slowly with V_{3T}. The transition between these two regimes creates a kink in the I–V curves at $V_{3T} \approx 0.3$ V. In the ideal case where the density of gap states g_{gap} is zero, $U_{barrier}$ remains constant, and the tunneling current becomes completely saturated (green, dashed line in figure 4(e)). In order to reproduce the experimental I–V we need to consider a nonzero density of gap states g_{gap}. For simplicity, we consider g_{gap} to be energy-independent (see SI, section 6) $g_{gap} = 1.8\%\ g_{2D}$, which leads to a nonideal current saturation (red, solid line). It is worth noting that in reality, g_{gap} is expected to be markedly energy-dependent, with a large density of gap states concentrated at energies near the conduction and valence band edges (further discussed in SI). An additional fitting parameter is the threshold gate voltage V_{th}, which shifts the position of $E_{F,S}$ with respect to E_C and thus determines the value of V_{3T} at which $E_{F,S} = E_C$. From the fit to the experimental I–V we get $V_{th} = 90$ V, well above the values extracted from four-terminal transfer characteristics. This indicates that the $MoSe_2$ flake is depleted by the proximity of the metallic contacts, as also discussed in section 3.

Figure 4(f) shows the experimental three-terminal I–V characteristics (markers) for different gate voltages V_g ranging from 30 to 60 V. The nonlinear 3T I–V curves show the tunneling diode behavior of the contact with forward negative bias. We fit the full set of I–V curves to equation (2) (solid lines), using g_{gap} as the only free parameter, while keeping A, B and V_{th} fixed. The full set of curves is well reproduced by the model considering a small density of gap states. The inset panel in figure 4(f) shows the values of g_{gap} extracted from the fits, increasing from $g_{gap} = 0.8\%\ g_{2D}$ at $V_g = 30$ V to $g_{gap} = 6\%\ g_{2D}$ at $V_g = 60$ V. This increase of g_{gap} for large gates voltages suggests that the density of gap states is indeed energy-dependent (rather than constant, as considered in the model, see SI), with a larger concentration of states

for energies close to the conduction band edge. In order to check the consistency of the values of g_{gap} extracted from the fits, we estimate its lower limit from the four-terminal transfer curves (with a V_g sweep of ± 60 V and $V_{th} = +20$ V). Assuming that switching from conduction to valence band requires at least a V_{gate} shift of 80 V, we get $g_{gap} \approx 1.5\%\ g_{2D}$, compatible with the values extracted from the model.

Figure 4(g) shows the contact resistance-area product ($R_C \cdot A$) as a function of V_g. The contact resistance (R_C) is defined as the resistance of the metal/SC interface plus the resistance of the SC channel beneath the contact [39]. We observe strong modulation of $R_C \cdot A$ as a function of V_g for the range of $V_g < 40$ V at high V_{sd}, which is not as large for low V_{sd}. Consistent with our explanation regarding the reverse (positive) bias of the Ti/h-BN/TMD tunneling diode, the positive V_{sd} lowers the E_F towards the SC bandgap, where changing the gate voltage can considerably tune the density of the sates. However, at very low V_{sd}, the E_F is still positioned in or close to the conduction band. Therefore the change in the density of states and so the contact resistance as a function of V_g is not as dramatic. The strong gate and bias dependence of the contact resistance and the tunneling current confirms efficient gating of the TMD channel beneath the contacts.

This gating effect of the bias applied on the contact is further evidenced by comparison of the two three-terminal (3T) measurement geometries, shown in figure 5(a). We also illustrate the resistor network of the metal/h-BN/TMD interface (in figure 5(b)), consisting of metal/h-BN/TMD contact resistance (in black), TMD channel beneath the contact (in blue) and TMD channel in between the two contacts (in green). In the 3T geometries, V^1_{3T} is the summation of the voltage drop on contact 2 (voltage on node N1 of figure 5(b)) and the voltage drop across the channel in between contact 1 and 2. The V^2_{3T} in this geometry measures the voltage of node N2 (of contact 2).

Measurement of V^1_{3T} and V^2_{3T} as a function of I_{sd} is compared in figure 5(c). As discussed, the channel resistance is order(s) of magnitude smaller than contact resistances. Therefore, the I–V characteristics from figure 5(c) are dominated by the voltage drop on the contact (C2) in both geometries. However, for almost all of the crossing contacts we observe distinct behavior of V^1_{3T} and V^2_{3T} for the positive range of the 3T voltages. Further, the deviation exactly occurs at the kink mentioned in the 3T I–V of figure 4(e), where the Fermi energy is below E_C. Such charge depletion underneath the contact makes the in-plane resistivity (blue resistors of figure 5(b)) to be comparable to the out-of-plane resistivity (black resistors). In this case the charge current that flows through the left side of the contact (node N1) is higher than that of the right side (node N2) and therefore the V^2_{3T} saturates to values lower than V^1_{3T}.

Figure 5(d) shows the shift of E_F with respect to E_C as a function of the three-terminal voltage for $V_g = V_{th} - 50$ V $= 40$ V. The kink in this diagram corresponds to the point at which the conduction band becomes fully depleted, closely matching the voltage at which the I–V curves from panel c start to diverge. Note that, as discussed above, even relatively small changes in V_{3T} can strongly modulate the doping of the channel. In particular, we observe that, even if the SiO_2 back gate is 50 V below the threshold voltage, a V_{3T} as small as -0.2 V is sufficient for E_F to reach the edge of the conduction band. Such considerable gating effect even at small biases due to the capacitor formed at the metal/bilayer h-BN contacts makes this contact geometry favorable for source-gated transistors [40, 41].

5. Conclusions

Our results show that metal/bilayer h-BN electrodes are very promising for low-energy transport in 1L TMD-based devices, allowing to reduce the effects of Fermi level pinning and formation of Schottky barriers. In consequence, we find that bilayer h-BN tunnel contacts outperform direct metal/SC contacts both in terms of electrical response and quality, yielding reduced hysteresis. Elimination of metal/TMD chemical interactions by the h-BN insertion layer along with the full BN-encapsulation of the channel and the side electrode geometry, allows to better preserve the intrinsic properties of the 2D channel and reach carrier mobilities comparable to those of the pristine $MoSe_2$ even at room temperature. The model described here for h-BN tunnel contacts to 2D semiconductors allows to satisfactorily describe and reproduce their experimental electrical response, showing that the doping of the semiconductor channel below the contacts can be largely modified even for relatively small source-drain bias voltages.

6. Methods

Atomically thin layers of $MoSe_2$ and h-BN are mechanically cleaved from their bulk crystals on SiO_2/Si substrates, using adhesive tapes [42]. We identify the thin flakes by their optical contrast with respect to the substrate [43, 44] and verify their thicknesses by atomic force microscopy (AFM). Using dry pick-up technique [27], we pick up the bilayer h-BN flake by PC (poly(bisphenol A)carbonate) and a PDMS stamp. We use the bilayer h-BN flake on the PC layer to pick up monolayer $MoSe_2$ by means of vdW interactions between the h-BN and $MoSe_2$ flakes. Then, we release the picked-up flakes on top of the bulk h-BN on SiO_2 (300 nm)/doped Si substrate, by melting the PC. The PC layer is dissolved in Chloroform for 5 min and the residues are removed by annealing the sample in Ar/H_2 flow at 350 C for 3 h. We proceed with fabrication of electrodes on the vdW stack by e-beam lithography technique (using PMMA as the e-beam resist) and e-beam evaporation of Ti (5 nm)/Au (75 nm) at the

pressure of 10^{-6} mbar, followed with lift-off in Acetone at 40 °C. The UHV condition for evaporation of the electrodes is to minimize interfacial contamination and more importantly to avoid oxidation of Ti.

Acknowledgments

We kindly acknowledge HM de Roosz, TJ Schouten, H Adema and JG Holstein for technical support. This research has received funding from the Dutch Foundation for Fundamental Research on Matter (FOM) as a part of the Netherlands Organisation for Scientific Research (NWO), FLAG-ERA (15FLAG01-2), the European Unions Horizon 2020 research and innovation programme under grant agreements No 696656 and 785219 (Graphene Flagship Core 1 and Core 2), NanoNed, the Zernike Institute for Advanced Materials, and the Spinoza Prize awarded to BJ van Wees by NWO.

ORCID iDs

Talieh S Ghiasi https://orcid.org/0000-0002-3490-5356

References

[1] Radisavljevic B, Radenovic A, Brivio J, Giacometti I V and Kis A 2011 *Nat. Nanotechnol.* **6** 147
[2] Schwierz F 2010 *Nat. Nanotechnol.* **5** 487
[3] Xiao D, Liu G B, Feng W, Xu X and Yao W 2012 *Phys. Rev. Lett.* **108** 196802
[4] Mak K F, McGill K L, Park J and McEuen P L 2014 *Science* **344** 1489–92
[5] Sanchez O L, Ovchinnikov D, Misra S, Allain A and Kis A 2016 *Nano Lett.* **16** 5792–7
[6] Das S, Chen H Y, Penumatcha A V and Appenzeller J 2012 *Nano Lett.* **13** 100–5
[7] Chen J R, Odenthal P M, Swartz A G, Floyd G C, Wen H, Luo K Y and Kawakami R K 2013 *Nano Lett.* **13** 3106–10
[8] Guo Y, Han Y, Li J, Xiang A, Wei X, Gao S and Chen Q 2014 *ACS Nano* **8** 7771–9
[9] Cui X *et al* 2017 *Nano Lett.* **17** 4781–6
[10] Avsar A, Tan J Y, Luo X, Khoo K H, Yeo Y, Watanabe K, Taniguchi T, Quek S Y and Ozyilmaz B 2017 *Nano Lett.* **17** 5361–7
[11] Kaushik N, Karmakar D, Nipane A, Karande S and Lodha S 2016 *ACS Appl. Mater. Interfaces* **8** 256–63
[12] Dankert A, Langouche L, Kamalakar M V and Dash S P 2014 *ACS Nano* **8** 476–82
[13] Lee S, Tang A, Aloni S and Philip Wong H S 2015 *Nano Lett.* **16** 276–81
[14] Wang J *et al* 2016 *Adv. Mater.* **28** 8302–8
[15] Allain A, Kang J, Banerjee K and Kis A 2015 *Nat. Mater.* **14** 1195
[16] Li S L, Komatsu K, Nakaharai S, Lin Y F, Yamamoto M, Duan X and Tsukagoshi K 2014 *ACS Nano* **8** 12836–42
[17] Gurram M, Omar S and van Wees B J 2017 *Nat. Commun.* **8** 248
[18] Bokdam M, Brocks G, Katsnelson M I and Kelly P J 2014 *Phys. Rev.* B **90** 085415
[19] Fabian J, Matos-Abiague A, Ertler C, Stano P and Žutić I 2007 *Acta Phys. Slovaca* **57** 565–907
[20] Farmanbar M and Brocks G 2015 *Phys. Rev.* B **91** 161304
[21] Farmanbar M and Brocks G 2016 *Adv. Electron. Mater.* **2** 1500405
[22] Wang X *et al* 2014 *ACS Nano* **8** 5125–31
[23] Chang Y H *et al* 2014 *ACS Nano* **8** 8582–90
[24] Dean C R *et al* 2010 *Nat. Nanotechnol.* **5** 722
[25] Joo M K, Moon B H, Ji H, Han G H, Kim H, Lee G, Lim S C, Suh D and Lee Y H 2016 *Nano Lett.* **16** 6383–9
[26] Ahn S, Kim G, Nayak P K, Yoon S I, Lim H, Shin H J and Shin H S 2016 *ACS Nano* **10** 8973–9
[27] Zomer P J, Guimarães M H D, Brant J C, Tombros N and van Wees B J 2014 *Appl. Phys. Lett.* **105** 013101
[28] Gong C, Zhang H, Wang W, Colombo L, Wallace R M and Cho K 2013 *Appl. Phys. Lett.* **103** 053513
[29] Britnell L *et al* 2012 *Nano Lett.* **12** 1707–10
[30] Ng K K 2002 *Complete Guide to Semiconductor Devices* (New York: Wiley)(https://doi.org/10.1002/9781118014769)
[31] Kang J, Liu W, Sarkar D, Jena D and Banerjee K 2014 *Phys. Rev.* X **4** 031005
[32] Late D J, Liu B, Matte H R, Dravid V P and Rao C 2012 *ACS Nano* **6** 5635–41
[33] Jin Z, Li X, Mullen J T and Kim K W 2014 *Phys. Rev.* B **90** 045422
[34] Quereda J, Castellanos-Gomez A, Agraït N and Rubio-Bollinger G 2014 *Appl. Phys. Lett.* **105** 053111
[35] Wang J I J, Yang Y, Chen Y A, Watanabe K, Taniguchi T, Churchill H O and Jarillo-Herrero P 2015 *Nano Lett.* **15** 1898–903
[36] Ando T, Fowler A B and Stern F 1982 *Rev. Mod. Phys.* **54** 437
[37] Chen J H, Jang C, Xiao S, Ishigami M and Fuhrer M S 2008 *Nat. Nanotechnol.* **3** 206
[38] Ponomarenko L, Belle B, Jalil R, Britnell L, Gorbachev R, Geim A, Novoselov K, Castro Neto A, Eaves L and Katsnelson M 2013 *J. Appl. Phys.* **113** 136502
[39] Cohen S S 1983 *Thin Solid Films* **104** 361–79
[40] Shannon J and Balon F 2008 *Solid-State Electron.* **52** 449–54
[41] Shannon J M, Sporea R A, Georgakopoulos S, Shkunov M and Silva S R P 2013 *IEEE Trans. Electron Devices* **60** 2444–9
[42] Novoselov K, Jiang D, Schedin F, Booth T, Khotkevich V, Morozov S and Geim A 2005 *Proc. Natl Acad. Sci. USA* **102** 10451–3
[43] Li H, Wu J, Huang X, Lu G, Yang J, Lu X, Xiong Q and Zhang H 2013 *ACS Nano* **7** 10344–53
[44] Benameur M, Radisavljevic B, Heron J, Sahoo S, Berger H and Kis A 2011 *Nanotechnology* **22** 125706